Enhancement of formic acid production from carbon dioxide hydrogenation using metal-organic frameworks

Monte Carlo simulation study

Wasik, Dominika O.; Martín-Calvo, Ana; Gutiérrez-Sevillano, Juan José; Dubbeldam, David; Vlugt, Thijs J.H.; Calero, Sofía

Important note
To cite this publication, please use the final published version (if applicable).
Please check the document version above.

Enhancement of formic acid production from carbon dioxide hydrogenation using metal-organic frameworks: Monte Carlo simulation study

Dominika O. Wasik [a,b], Ana Martín-Calvo [c], Juan José Gutiérrez-Sevillano [c], David Dubbeldam [d], Thijs J.H. Vlugt [e], Sofía Calero [a,b,*]

[a] Materials Simulation and Modelling, Department of Applied Physics, Eindhoven University of Technology, 5600MB Eindhoven, The Netherlands
[b] Eindhoven Institute for Renewable Energy Systems, Eindhoven University of Technology, PO Box 513, Eindhoven 5600 MB, The Netherlands
[c] Department of Physical, Chemical, and Natural Systems, Universidad Pablo de Olavide, Ctra. Utrera km. 1, 41013 Seville, Spain
[d] Van't Hoff Institute for Molecular Sciences, University of Amsterdam, 1098XH Amsterdam, The Netherlands
[e] Engineering Thermodynamics, Process & Energy Department, Faculty of Mechanical, Maritime and Materials Engineering, Delft University of Technology, Leeghwaterstraat 39, Delft 2628CB, The Netherlands

ARTICLE INFO

ABSTRACT

Formic acid production from CO_2 allows the reduction of carbon dioxide emissions while synthesizing a product with a wide range of applications. CO_2 hydrogenation is challenging due to the cost of transition metal catalysts and the toxicity of the transition elements. In this work, the thermodynamic confinement effects of the metal–organic framework UiO-66 on the CO_2 hydrogenation to formic acid were studied by force field-based molecular simulations. The confinement effects of UiO-66 and the metal–organic frameworks Cu-BTC, and IRMOF-1 were compared, to assess the impact of different pore size and metal centers on the production of HCOOH. Monte Carlo simulations in the grand-canonical ensemble were performed in the frameworks, using gas phase mole fractions of CO_2, H_2, and HCOOH at chemical equilibrium, obtained from Continuous Fractional Component Monte Carlo simulations in the Reaction Ensemble. The adsorption isobars of the components in metal–organic frameworks were computed at 298.15 – 800 K, 1 – 60 bar. The enhancement of HCOOH production due to preferential adsorption of HCOOH in metal–organic frameworks was calculated for all studied conditions. UiO-66, Cu-BTC, and IRMOF-1 affect CO_2 hydrogenation reaction, shifting the thermodynamical equilibrium toward HCOOH formation. The prevailing factor is the type of metal center in the metal–organic framework. The confinement effect of Cu-BTC turns out to exceed the enhancement caused by UiO-66, and IRMOF-1. The resulting mole fraction of HCOOH increased by ca. 2000 times compared to the gas phase at 298.15 K, 60 bar. Cu-BTC can be considered as an alternative to improve the production of HCOOH due to elimination of the high-cost temperature elevation, cost reduction of downstream processing methods, and comparable final concentration of HCOOH to the reported concentrations of formate obtained using transition metal catalysts.

1. Introduction

Since the beginning of the industrial era in 1750, the carbon dioxide level in the atmosphere has increased from ca. 277 parts per million (ppm) [1] to ca. 412.4 ppm in 2020 [2]. Technological efforts are made to reduce CO_2 emissions by the capture at the source and conversion to useful feedstock chemicals, e.g., formic acid, methanol, propylene, urea, polyols and salicylic acid [3–6]. Formic acid (HCOOH) has a large variety of applications. HCOOH is used as a potential hydrogen carrier [7], an antibacterial and preservative agent in livestock feed [8, 9], in the process of leather tanning and textiles dyeing [10], the

production of rubber [11], and for the hydrothermal decarbonylation and decarboxylation in the water-gas-shift reaction [12]. The market value of HCOOH is expected to increase from 1.5 billion dollars to 4 billion dollars in the next 10 years [13], which corresponds to the increase in the expected market demand. One of the methods for producing HCOOH is the electrochemical reduction of CO_2 in an aqueous electrolyte solution [14–18]. The electrocatalytic reduction of CO_2 to HCOOH has disadvantages due to the low solubility of CO_2 in aqueous solutions, being a consequence of salting-out effects [19].

The possible solutions to increase the yield of the process include high-cost elevation of the CO_2 pressure [15] or the use of a gas diffusion electrode, but in this case fouling and/or undesired crystallization takes place [20–22].

The hydrogenation of CO_2 into HCOOH is challenging due to the high kinetic and thermodynamic stability of CO_2 [23]:

$$CO_2 + H_2 \rightleftharpoons HCOOH \tag{1}$$

The carbon atom in CO_2 is in the highest formal oxidation state (+4) [24]. In a study by Ghara et al. [24], the free energy change for CO_2 hydrogenation to HCOOH was computed as 41.84 kJ mol^{-1}. The free energy barrier of CO_2 hydrogenation in the gas phase was found to be 351.46 kJ mol^{-1}. This high value indicates that the use of catalyst is needed to mediate the reduction. Over the past few decades, transition metal based catalysts for CO_2 hydrogenation have been developed. The most efficient catalytic systems consist of catalysts with phosphine ligands [25–29], pincer ligands [30–32], N-heterocyclic carbene ligands [33–35] and half-sandwich catalysts with/without proton-responsive ligands [36–40]. The cost of transition metal catalysts and the toxicity of the transition elements are two major limitations in their usage [24]. It is therefore crucial to investigate the possibilities of improving the CO_2 hydrogenation efficiency with a simultaneous decrease of cost and toxicity. Attempts to design transition metal-free homogeneous catalysts have been made by, e.g. studies on the potential application of frustrated Lewis pairs (FLPs) [24,41,42]. The FLPs have the ability to activate small, and stable molecules as an alternative strategy. In a study by Stephan et al. [41], it was shown that $B(C_6F_5)_3$ and tBu_3P in C_6H_5Br can bind CO_2 reversibly under mild conditions. The activation of H_2 and insertion of CO_2 into a B-H bond in the first homogeneous process for hydrogenation of CO_2 to CH_3OH was presented in a study by Ashley et al. [42] However further investigation on the stability of the system was necessary. The first catalytic process of CO_2 hydrogenation to formate in the presence of transition metal-free catalyst (BCF/M_2CO_3, M = Na, K, and Cs) was disclosed by Zhao et al. [43], resulting in high turnover number (ca. 4000). The confinement effect of porous materials on the thermodynamical equilibrium of the reaction may also be considered as an alternative to the transition metal catalysts. The effects of confinement that might affect reaction equilibrium are: (a) the higher density of pore phase compared to the bulk-phase, resulting in an increase in yield for reactions in which there is a decrease in the total number of moles, by Le Chatelier's principle [44], (b) vicinity of the neighboring pore walls affecting the molecular orientation, (c) the selective adsorption of favored components on the solid surfaces [45]. The interactions between the framework and the adsorbates result in favoring some components and disfavoring others. The separation of favored components from the other components of the mixture causes their enhanced formation by Le Chatelier's principle [44]. Previous studies on the reactions carried out in confinement showed a shift in the thermodynamic equilibrium [45–51].

Metal–organic frameworks (MOFs) are a class of porous materials that contain organic ligands and metal clusters linked by coordination bonds [52]. The high density of catalytic sites in high-area porous solids and the controllable porous structure initiated intensive research in the area of MOFs [53–55]. The main goal is preparing new MOF structures to investigate their applications mainly in gas storage [56] and separation [57]. Recently, MOFs have gained attention as potential catalysts [58–62]. The application of MOFs in catalysis has already been successful, e.g., in a process of methane reforming [63], palladium-catalyzed reactions (alcohol oxidation, Suzuki C–C coupling, and olefin hydrogenation) [58], and isomerizations of terpenes, terpene epoxides, and ketals [59]. MOF-based catalysts show a better economic performance, recyclability, longer life span, and relatively lower carbon emissions than previously used Ni-based catalysts [63, 64]. In the study of Ong et al. [63], MOF-based catalysts were considered as an alternative to conventional transition metal catalysts in dry methane reforming. These catalysts have net present values of ca. 62%, 140%, and 560% higher than Ni-Ce/Al_2O_3, Ni/Al_2O_3, and Ni-HTNT, respectively, and carbon emissions of ca. 13%, 20%, and 76% lower than Ni/Al_2O_3, Ni-HTNT, and unsupported Ni, respectively. The potential advantages of MOF-based catalysts include easier catalyst separation, recycling, and recovery of a product, reduced cost of the catalyst due to metal-free catalytic sites, high thermal stability, the combination of CO_2 capture and conversion steps, pore-confinement effects, and mild conditions of CO_2 reduction due to low reaction barriers [64]. There is a considerable interest in a metal–organic framework UiO-66 due to its superior mechanical, thermal, acidic, aqueous, and water vapor stability, high porosity, and catalytic properties of the zirconium oxide node and an easy lab-scale synthesis [65]. UiO-66 is a framework containing metal nodes composed of a zirconium oxide complex bridged by terepthalic acid (1,4-benzenedicarboxylic acid) ligands [65]. The adsorption of H_2 and CO_2 in UiO-66 was studied experimentally [52,66] and computationally [67]. As a result, UiO-66 has been determined as an effective adsorbent with an adsorption of H_2 as high as 4.2 wt% at 60 bar, 77 K, and CO_2 adsorption of 35.6 wt% at 9.8 bar and 273 K [52,68]. The adsorption performance of both reactants makes the application of UiO-66 in the CO_2 hydrogenation to HCOOH potentially promising. To the best of our knowledge, there are no literature data regarding the confinement effect of UiO-66 on the production yield of HCOOH from CO_2 and H_2. In a study by Ye and Johnson [64,69], the catalytic activity of functionalized UiO-66 toward CO_2 hydrogenation was evaluated based on reaction energies, barriers, and geometries for the CO_2 reduction steps, computed using Density Functional Theory (DFT). Several non-metal frustrated Lewis pairs were incorporated into the linkers of the MOF. The ease of recovery, high mass transfer, and low reaction barriers make the application of the catalysts potentially promising [64,69]. UiO-66 was also found to be an effective catalyst for CO_2 hydrogenation to CH_3OH [70]. In a study by Yang and Jiang [70], the defective UiO-66 with a frustrated Lewis pair was successfully used in a three-stage transformation of CO_2: (a) CO_2 hydrogenation to HCOOH, (b) HCOOH conversion to formaldehyde (HCHO), (c) HCHO hydrogenation to CH_3OH [70]. Given the literature data on the catalytic activity of UiO-66, an interesting research topic is to verify whether its confinement effect causes a shift in the thermodynamic equilibrium of the CO_2 hydrogenation to HCOOH. The "confinement effect" should be studied independently from the "catalytic effect", otherwise it is unclear what is caused by confinement, and what is caused by catalysis. Molecular simulations are a natural tool that allows us to "switch off" the catalysis and exclusively consider the confinement effects. The resulting shift in the thermodynamic equilibrium of the CO_2 hydrogenation can be evaluated by comparison to the gas phase studied at 400–1400 K and 1 bar [71]. In this work, the effect of UiO-66 confinement on the CO_2 hydrogenation reaction is studied at less industrially expensive temperatures 298.15–800 K and higher pressures 1 - 60 bar, which allow more molecules to enter the structure. The results were compared with the confinement effects of metal–organic frameworks Cu-BTC and IRMOF-1 to assess the impact of different pore size and metal centers on CO_2 hydrogenation reaction.

This manuscript is organized as follows: in Section 2, we provide technical details of the molecular simulation methods. In Section 3, we define the metal–organic frameworks, and the force fields for CO_2, H_2 and HCOOH. In Section 4, we provide detailed information on the simulations. In Section 5, we present and discuss the results. The adsorption isobars are computed by Monte Carlo simulations in the grand-canonical ensemble, using the initial CO_2, H_2 and HCOOH mole fractions at reaction equilibrium obtained from Continuous Fractional Component Monte Carlo simulations [72–74] in the Reaction Ensemble [75–77]. The HCOOH production enhancement is calculated for all systems. The effects of UiO-66, Cu-BTC, and IRMOF-1 confinement are shown to increase the HCOOH production. Our findings are summarized in Section 6.

2. Methodology

The confinement effect by Le Chatelier's principle on the thermodynamic equilibrium of the studied reaction is analyzed using force field-based molecular simulations. The catalytic effects are absent in our model, and we fully focus on the equilibrium thermodynamics of the chemical reaction. We use the Monte Carlo (MC) Software Brick-CFCMC [78,79] and the RASPA software package [80,81] to perform simulations in the bulk-phase and confinement, respectively. Continuous Fractional Component Monte Carlo simulations [72–74] in the Reaction Ensemble [75–77] (Rx/CFC) were used to simulate the thermodynamic equilibrium of CO_2 hydrogenation reaction in the bulk-phase. In the Monte Carlo simulations in the Reaction Ensemble (RxMC), the reactants and products are interconverted using a series of stochastic trial moves [82]. The insertion and deletion of the reactants and reaction products during Monte Carlo (MC) trial moves in RxMC propagate the system to thermodynamic equilibrium. The activation energy barriers related to transition states are not considered as the dimension time is absent in the simulations [82]. The application of RxMC in reaction equilibrium predictions was already successful for many systems [45,71,83–87]. The RxMC technique is difficult to apply for high density systems since it critically relies on insertion and deletion of reactants and reaction products [77]. To improve the acceptance probabilities for insertion and deletion trial moves in RxMC, the Continuous Fractional Component Monte Carlo (CFCMC) method [72–74,77] is applied. Fractional molecules are introduced to the system and their interactions with the surroundings are scaled by a parameter $\lambda \in [0,1]$. When $\lambda = 0$, fractional molecules are considered as ideal gas molecules. For $\lambda = 1$, fractional molecules have the same interactions with the surroundings as the other molecules (not being a fractional molecule). The surroundings can easily adapt to the inserted/deleted molecules, which is of particular importance at high densities (e.g., computation of the loading and enthalpy of adsorption of guest molecules in porous materials near the saturation loading [88] and reaction equilibria of complex systems [89]). The chemical reaction is a MC trial move to ensure chemical reaction equilibrium. The required ideal-gas partition functions in combination with the medium/surrounding of molecules effects are used to describe the chemical reaction equilibrium [77]. The force field describing interactions between molecules, the ideal gas partition functions of all reactants and reaction products, and the stoichiometry of the chemical reactions in the system are used as input for Rx/CFC simulations [77]. The stoichiometry of the studied CO_2 hydrogenation (Eq. (1)) is 1:1:1 for CO_2:H_2:HCOOH. The ideal gas partition functions were obtained based on the vibrational and rotational experimental data from the NIST database [90–94], see Table S1 of the Supporting Information. For details about computation and prediction of ideal-gas partition functions the reader is referred to the book by McQuarrie et al. [95]. To validate our approach, the equilibrium composition of syngas from the study of Rahbari et al. [71] was reproduced assuming the ideal gas behavior by Rx/CFC simulations, see Figure S1 of the Supporting Information. The composition of the systems studied in this work by Rx/CFC simulations consists of equal number of CO_2 and H_2 molecules (200) according to the stoichiometry of the CO_2 hydrogenation reaction. Simulations were performed at 298.15–800 K and 1–60 bar.

The next step is to investigate the effect of UiO-66 on the equilibrium of the CO_2 hydrogenation reaction. The combination of the force fields of HCOOH and MOFs cannot be investigated due to the lack of adsorption data available. For the estimation, the compatibility of the HCOOH force field with the framework was validated by simulating the HCOOH density in the pores of the framework close to the maximum loading and comparing to the experimental data. It is necessary to compute the helium void fraction (ξ) of the framework to perform simulations of the system in confinement. This is required to calculate the HCOOH density taking into account the empty space of a structure. These simulations use a probe helium atom exploring the structure using Widom's particle insertion method to measure the energy required for insertion of the particle in the system or the energy obtained by inserting the particle [80,96]. The computed value of the ξ was compared to literature data [97]. To reach the maximum pore loading, the GCMC simulation of HCOOH adsorption in UiO-66 was performed at low temperature (77 K, 1000 bar). The obtained density of HCOOH was compared to the experimental [98] and simulated [18] density of liquid HCOOH. The HCOOH density at the maximum pore loading in units of kg m^{-3} was calculated by:

$$\rho = \frac{M \cdot N}{\xi \cdot V \cdot N_A} \tag{2}$$

where M is the molar mass of HCOOH in units of kg mol^{-1}, N is the number of molecules in the unit cell, ξ is the helium void fraction, V is the volume of the UiO-66 unit cell in units of m^3, and N_A is Avogadro's constant.

The adsorption isobars of the studied systems were computed from Monte Carlo simulations in the grand-canonical ensemble (GCMC) [99]. In the GCMC ensemble, the chemical potential, volume, and temperature are fixed. The mole fractions of CO_2, H_2 and HCOOH at the reaction equilibrium obtained from Rx/CFC simulations were used in the GCMC simulations as the input data. The fugacity coefficients are computed using the Peng-Robinson Equation of State (PR-EoS) [100] to convert pressure to fugacity, using the RASPA software package [80, 81]. The chemical potential is directly obtained from the fugacity as follows [80]:

$$\beta\mu_i = \beta\mu_{i0} + \ln\left(\frac{f_i}{P_0}\right) \tag{3}$$

where μ_i is the chemical potential of component i for a non-ideal gas, $\beta = 1/(k_B T)$, f_i is the fugacity of component i, P_0 is the reference pressure equal to 1 bar, μ_{i0} is the chemical potential of component i in the reference state. The initial mole fractions and fugacity coefficients are listed in Tables S4 and S5 of the Supporting Information. The fugacity coefficients for the mixtures of CO_2, H_2, and HCOOH computed using the Peng-Robinson equation of state [100] were compared with the fugacity coefficients for binary mixtures of CO_2, and H_2 obtained from the NIST Standard Reference Database REFPROP [101]. Very good agreement between the computed fugacity coefficients and the database is shown in Table S5 of the Supporting Information. The mole fractions obtained from Rx/CFC simulations are used as input in simulations in the GCMC ensemble, as in the study by Matito-Martos et al. [102]

To calculate the standard deviations of the computed number of molecules in the bulk-phase, the Brick-CFCMC simulations were performed five times starting from independent configurations and using different random number seeds. The algorithms provided in Brick-CFCMC [78,79] are used to generate random initial configurations. The uncertainties in the computed number of molecules adsorbed in a unit cell were provided by the RASPA software package [80] and were used in the case of simulations in UiO-66. The simulation is divided into five blocks and the error is computed by calculating the standard deviation. Due to the high uncertainties in simulations using Cu-BTC and IRMOF-1, the simulations in both the MOFs were performed five times to calculate the standard deviations of the computed number of molecules adsorbed in the confinement. The uncertainty of the HCOOH density at the maximum pore loading (Err_ρ) is calculated based on error propagation [103]:

$$Err_\rho = \frac{M}{V \cdot N_A} \cdot \rho \cdot \sqrt{\left(\frac{Err_N}{N}\right)^2 + \left(\frac{Err_\xi}{\xi}\right)^2} \tag{4}$$

where M is the molar mass of HCOOH, V is the average volume of the UiO-66 unit cell, N_A is Avogadro's constant, N is the number of molecules in the unit cell, ξ is the helium void fraction, ρ is the HCOOH density, Err_N is the uncertainty of the computed number of molecules adsorbed in a unit cell, and Err_ξ is the uncertainty of the helium void fraction.

The uncertainties in the obtained mole fractions are expressed by Err_x and calculated as:

$$Err_{\sum N} = \sqrt{Err_{N_{CO_2}}{}^2 + Err_{N_{H_2}}{}^2 + Err_{N_{HCOOH}}{}^2} \qquad (5)$$

$$Err_x = x \cdot \sqrt{\left(\frac{Err_N}{N}\right)^2 + \left(\frac{Err_{\sum N}}{\sum N}\right)^2} \qquad (6)$$

where Err_N is the uncertainty of the computed number of molecules adsorbed in a unit cell, $Err_{\sum N}$ is the uncertainty of the total number of molecules of all components adsorbed in a unit cell, x is a mole fraction of the component, and N is the computed number of molecules of the component.

To analyze the resulting production of HCOOH, the interactions between an adsorbate molecule and the framework were studied. The isosteric heat of adsorption [104] was computed for CO_2, H_2 and HCOOH in UiO-66 at 298.15–800 K. The affinity of the molecule with the framework can be expressed as the binding energy. The enthalpy of adsorption at infinite dilution is calculated by [105]:

$$\Delta H = \Delta U - RT = \langle U_{hg} \rangle - \langle U_h \rangle - \langle U_g \rangle - RT \qquad (7)$$

where ΔU is the internal energy of the system, $\langle U_{hg} \rangle$ is the average energy of the guest molecule inside the host framework, $\langle U_h \rangle$ is the average energy of the host framework which is equal to 0 J for rigid frameworks, $\langle U_g \rangle$ is the average energy of the guest molecule which is equal to 0 J for rigid molecules, R is the universal gas constant and T is the temperature.

To compare the mole fractions of HCOOH obtained from GCMC simulations to the bulk-phase at the same chemical potential, the enhancement (*ENH*) of HCOOH production is calculated as:

$$ENH = \frac{x_{GCMC}}{x_{Rx/CFC}} \qquad (8)$$

where x_{GCMC} and $x_{Rx/CFC}$ are mole fractions of HCOOH obtained from GCMC simulations and Rx/CFC simulations, respectively. The pore size distributions of the studied UiO-66, Cu-BTC, and IRMOF-1 frameworks were computed to analyze, whether the enhancement in the production of HCOOH in MOFs results from increased confinement or different metal centers, see Figure S2 of the Supporting Information.

3. Force field

The guest–host and guest–guest intermolecular interactions are modeled by Coulombic and Lennard-Jones (LJ) interaction potentials, except for the interaction between C and O atoms of CO_2 molecules that are specified by an override. The Lorentz–Berthelot mixing rules [106] are used to define interactions between unlike Lennard–Jones sites. Explicit polarization effects are neglected and accounted for in the LJ interactions. The so-called 'P2' variant of the OPLS/AA force field for HCOOH from the study of Salas et al. [107] was used. The HCOOH molecule was constructed and its geometry was optimized at the B3LYP/6-31G(d) level of theory [18]. The interaction sites of the model are at the atom positions. The cutoff radius for intermolecular interactions is set to 12 Å. In the Rx/CFC simulations, LJ interactions are truncated with analytic tail corrections applied. In the GCMC simulations, LJ interactions are cut and shifted to zero at the cutoff with the tail corrections omitted, due to the generic force field for MOFs being used. Periodic boundary conditions are exerted in all three directions. The Ewald summation method [108] is used for calculating electrostatic interactions. The Ewald summation method parameters correspond to a relative precision of 10^{-6}. The so-called 'P2' variant of the OPLS/AA force field for HCOOH [107] was validated in our previous work [18] by reproducing the vapor–liquid equilibrium coexistence curve, saturated vapor pressures, and densities at different temperatures. The interaction parameters of the HCOOH force field are used in this work together with the three-site charge-quadrupole model

Table 1

LJ interaction parameters for the UiO-66, Cu-BTC, and IRMOF-1 frameworks [111,112], a probe helium atom [117], HCOOH [107], CO_2[110], and H_2[109]. It is important to note that there is an exception/override for CO_2 atoms to the use of the Lorentz–Berthelot mixing rules. Figure S3 of the Supporting Information shows a schematic representation of the HCOOH model with all atoms labeled.

Atom	ϵ/k_B /[K]	σ /[Å]	q /[e$^-$]
He	10.9	2.64	0
O_{CO_2}	85.671	3.017	−0.3256
C_{CO_2}	29.93	2.742	0.6512
C_{fa1}	49.6728	3.67	0.52
O_{fa2}	99.34559	2.9	−0.44
H_{fa1}	7.09611	2.37	0
O_{fa1}	80.46271	2.94	−0.53
H_{fa2}	1	1	0.45
H_{com}	36.7	2.958	−0.936
H_{H_2}	0	0	0.468
UiO-66			
Zr	34.7221	2.78317	4.503
C1	47.86	3.473	0.529571
C2	47.86	3.473	0.0131923
C3	47.86	3.473	−0.137721
O1	48.19	3.0331	−0.739224
O2	48.19	3.0331	−3.30054
H1	7.65	2.8464	0.0373778
H2	7.65	2.8464	0.241634
Cu-BTC			
Cu	2.518	3.114	1.248
O	48.19	3.0331	−0.624
C1	47.86	3.473	0.494
C2	47.86	3.473	0.13
C3	47.86	3.473	−0.156
H	7.65	2.8464	0.156
IRMOF-1			
Zn	27.7	4.04	1.275
O1	48.19	3.0331	−1.5
O2	48.19	3.0331	−0.6
C1	47.86	3.473	0.475
C2	47.86	3.473	0.125
C3	47.86	3.473	−0.15
H	7.65	2.8464	0.150
override			
O_{CO2} - C_{CO2}	50.64	2.88	

by Darkrim and Levesque for H_2[109] and the García-Sánchez et al. force field for CO_2[110]. The models of the framework and guest–host interaction used in this work are rigid, and all atoms of the molecules have point charges assigned. The atomic positions of HCOOH, CO_2, and H_2 molecules are listed in Table S2 of the Supporting Information. The structures of triclinic UiO-66, cubic Cu-BTC, and cubic IRMOF-1 crystal systems are rigid, with the atoms of the frameworks at crystallographic positions. The UiO-66, Cu-BTC, and IRMOF-1 cell parameters are listed in Table S3 of the Supporting Information. LJ parameters for the atoms of the framework are from the DREIDING force field [111], except for zirconium and copper, which is from the UFF force field [112]. The force fields for UiO-66, and Cu-BTC containing parameters from DREIDING, and UFF were already validated with experimental data by Jajko et al. [97], Frost et al. [105], Dubbeldam et al. [113], Jajko et al. [114], and Gutiérrez-Sevillano et al. [115] Point charges for UiO-66 were obtained using the EQeq method [116] and modified as in the study of Jajko et al. [97] The atomic charges for the Cu-BTC and IRMOF-1 were taken from Frost et al. and Dubbeldam et al. [113] The LJ parameters and partial charges for all components, the framework and the probe helium atom [117] used in this work are listed in Table 1.

4. Simulation details

Each simulation in the Rx/CFC ensemble was carried out with $5 \cdot 10^4$ equilibration cycles. In the production phase, 10^6 MC cycles were performed. One single MC cycle consists of N MC trial moves, where N is the total number of molecules at the start of the simulation. The probabilities for selecting trial moves in Rx/CFC simulations were: 24.8% translations, 24.8% rotations, 0.8% volume changes, 24.8% CFC λ change trial moves [78], and 24.8% Reaction Ensemble trial moves [77], in which reactants are removed and reaction products are inserted in the system, in a such way that an equilibrium distribution of reactants and reaction products is obtained. The GCMC simulation of the HCOOH density at the maximum pore loading, used for the model validation, consisted of 10^4 equilibration MC cycles and $1.495 \cdot 10^5$ production MC cycles. The GCMC simulations of the adsorption of CO_2, H_2, and HCOOH in MOFs were carried out with $1 \cdot 10^4$ equilibration cycles, and $4 \cdot 10^5$ MC production cycles. The probabilities of selecting trial moves in GCMC simulations were 16.7% translations, 16.7% rotations, 16.7% reinsertions, 16.7% identity changes (changing the identity of the selected molecule) and 33.2% swap trial moves (exchanging molecules with the reservoir). The simulations of the enthalpy of adsorption at infinite dilution were carried out with $1 \cdot 10^5$ initialization cycles and $1 \cdot 10^5$ production cycles.

5. Results and discussion

We first computed the helium void fraction of UiO-66, which is used to calculate the HCOOH density. The obtained value equals 0.5070 ± 0.0002 and agrees with literature data (0.5071 [97]). The compatibility of HCOOH with the framework was tested by computing the density of HCOOH at the maximum pore loading. The computed value of the density was found to be ca. 1073 kg m^{-3} at 77 K and 1000 bar. There is a relative difference of 12% between the computed value and the experimental density of the liquid HCOOH at 293.15 K [98] (1220 kg m^{-3}) and a relative difference of 9% compared to the simulated value of the HCOOH density in the bulk-phase at 298.15 K from our previous work [18] ($1177 \pm 1 \text{ kg m}^{-3}$). The differences between the HCOOH density at the maximum pore loading and in the bulk-phase are due to the relatively large size of the HCOOH molecule compared to the pore size of UiO-66 and the formation of hydrogen bonds between HCOOH and the framework. There are two types of micropores with a diameter at 3.5 Å and 7 Å present in the UiO-66 structure, see Figure S2 of the Supporting Information. The length between the most distant HCOOH atoms (H_{fa1} and H_{fa2}) is 2.804 Å and can affect the adsorption, which is the most consequential at low pressure.

Before studying the effect of the UiO-66 on the reaction yield, we simulated the CO_2 hydrogenation reaction in the gas phase at 298.15–800 K and 1–60 bar. In Fig. 1, the mole fractions of HCOOH computed from the Rx/CFC simulations at 1 bar were compared to literature values calculated from equilibrium constants of the CO_2 hydrogenation reaction from the study of Rahbari et al. [71]. The isobars of simulated and calculated mole fractions of HCOOH overlap within the error bars. The results were obtained with high accuracy even when the values are of the order of magnitude 10^{-8}. It was shown that the simulations reproduce the mole fractions of HCOOH calculated from the literature [71].

The HCOOH reaction yield obtained from the Rx/CFC simulations at 298.15–800 K and 1–60 bar is shown in Fig. 2. The obtained mole fractions of all components in the system are listed in Table S4 of the Supporting Information, respectively.

The production of HCOOH from the uncatalyzed CO_2 hydrogenation turns out to be challenging, as low amount of product is obtained — the mole fractions of HCOOH are of the order of magnitude 10^{-6}. Increasing the temperature from 298.15 K to 800 K has an effect on the resulting mole fraction of FA: it increases approximately 13.2 times in all the studied systems. The reaction of CO_2 hydrogenation requires
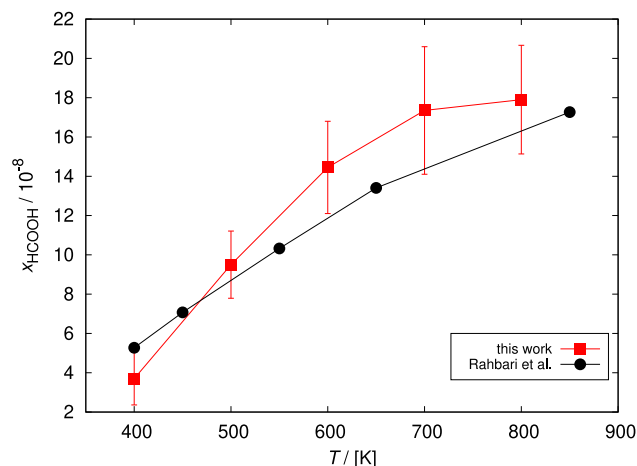

Fig. 1. HCOOH mole fractions computed from the Rx/CFC simulations in the bulk-phase and calculated from equilibrium constants of CO_2 hydrogenation reaction from the study of Rahbari et al. [71]. The Rx/CFC simulations were carried out at 400–800 K and 1 bar. As the equilibrium constants reported in the study of Rahbari et al. [71] lack uncertainty values, it is assumed that the isobars of simulated and calculated HCOOH mole fractions overlap within the error bars.
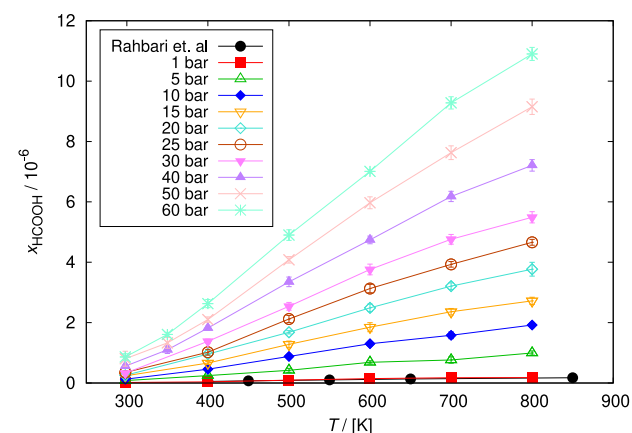

Fig. 2. HCOOH mole fractions computed from the Rx/CFC simulations in the bulk-phase. The mole fractions of HCOOH computed from the Rx/CFC simulations at 1 bar were compared to literature values, calculated from equilibrium constants of CO_2 hydrogenation reaction from the study of Rahbari et al. [71]. The simulations were carried out at 298.15–800 K and 1–60 bar. The mole fractions of HCOOH increase with temperature and pressure. The order of magnitude for the uncertainties are ranging from $1 \cdot 10^{-9}$ to $1 \cdot 10^{-7}$.

energy to be driven, due to its endergonicity (the free energy change is equal to $41.84 \text{ kJ mol}^{-1}$ [24]). The HCOOH mole fraction increases approximately 56 times with pressure in the range from 1 bar to 60 bar. When the pressure increases, the reaction proceeds in that direction in which the volume decreases, by Le Chatelier's principle [44]. The highest HCOOH mole fraction, obtained at 800 K and 60 bar, is equal to $1.09 \cdot 10^{-5}$. The order of magnitude for uncertainty values is from $1 \cdot 10^{-9}$ to $1 \cdot 10^{-7}$.

In Fig. 3, the location of the equilibrium of the CO_2 hydrogenation in the gas phase is shown as a function of T and P. The color code of the scale is the mole fraction of HCOOH starting from an equimolar mixture of CO_2 and H_2. The presence of orange color at 800 K and 60 bar indicate the highest production of HCOOH, equal to $1.09 \cdot 10^{-5}$. The conditions in which the mole fraction of HCOOH reaches the equivalent values are possible to distinguish: a similar result can be obtained, e.g., at 800 K, 30 bar and 500 K, 60 bar. This comparison can be useful when there is a need to lower the production temperature for economic reasons.
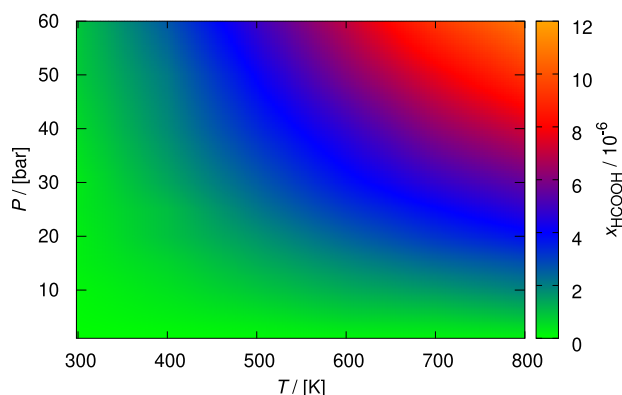
Fig. 3. Location of the equilibrium of the CO_2 hydrogenation in the gas phase as a function of T and P. The color gradation on the scale relates with the highest and lowest production of HCOOH. The highest production of HCOOH equal to $1.09 \cdot 10^{-5}$ is obtained at 800 K and 60 bar. The mole fractions of HCOOH increase with temperature and pressure, due to the endergonicity of CO_2 hydrogenation reaction and Le Chatelier's principle, respectively. (For interpretation of the references to color in this figure legend, the reader is referred to the web version of this article.)
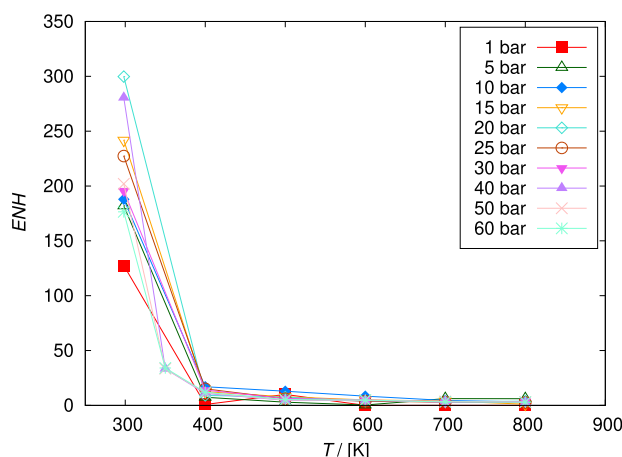

Fig. 4. Enhancement (*ENH*, Eq. (8)) in the production of HCOOH obtained from GCMC simulations in UiO-66 framework. The simulations were carried out at 298.15–800 K and 1–60 bar. The mole fractions of HCOOH computed from the Rx/CFC simulations (see Table S4 of the Supporting Information) are used as an input for GCMC ensemble. The mole fractions obtained from GCMC simulations are listed in Table S6 of the Supporting Information. The enhancement in HCOOH production decreases with increasing temperature. HCOOH production increases ca. 37 times compared to the gas phase for all studied conditions. The resulting value at 800 K and 1 bar was discarded due to high uncertainty.

An attempt to improve HCOOH production was made by studying the effect of a confinement on the equilibrium of the CO_2 hydrogenation. GCMC simulations were carried out using the mole fractions of the components from the Rx/CFC simulations in the bulk-phase. The mole fractions obtained from GCMC simulations are listed in Table S6 of the Supporting Information. In Fig. 4, the HCOOH production enhancement (*ENH*, Eq. (8)) obtained from GCMC simulations in the UiO-66 framework is shown.

The effect of the UiO-66 confinement caused an average enhancement in HCOOH production by ca. 37 times compared to the gas phase. The enhancement in HCOOH production decreases with increasing temperature from approximately 212 at 298.15 K to 3 at 800 K. The most efficient conditions resulting in the highest mole fraction of HCOOH are at 298.15 K, 60 bar. The confinement effect of UiO-66 increases the HCOOH production by 176 times compared to the gas phase. The obtained mole fraction of HCOOH equals to $1.5 \cdot 10^{-4}$. Figure S4 of the Supporting Information shows that the HCOOH mole fractions

increase with pressure and decrease with the increasing temperature. The increasing pressure allows more molecules to enter the structure and fill the pores. The temperature has an opposite effect on mole fractions of HCOOH obtained in UiO-66 comparing to the bulk-phase. In the confinement, the exothermic reaction of CO_2 hydrogenation does not require energy to be absorbed from the surroundings, the enthalpy change has a negative value. There is a sharp drop in the mole fractions of HCOOH from 298.15 K to 400 K - the values decrease ca. 6 times in the pressure range from 1 to 60 bar. Above 400 K, mole fractions of HCOOH does not decrease. At 1 bar, HCOOH is produced only up to 500 K. Above 500 K, the HCOOH mole fraction values are equal to 0 within the error bars. Although all the mole fractions of HCOOH obtained in the UiO-66 framework are of the order of magnitude 10^{-6} - 10^{-4}, the increase up to 300 times comparing to the bulk-phase was observed. This increase in the mole fraction of HCOOH points to the existing effect of UiO-66 on the CO_2 hydrogenation reaction. This effect is most likely extendable to lower temperatures and higher pressures. Further studies at these conditions are needed to investigate the maximum production of HCOOH to be obtained using UiO-66. We found that UiO-66, that was characterized by high CO_2 and H_2 adsorption [52,66,67], has positive influence on the CO_2 hydrogenation reaction due to the increased formation of a favored HCOOH product.

The adsorption of CO_2 and H_2 in UiO-66 is shown in Fig. 5. The highest mole fraction of CO_2 is obtained at 298.15 K and 1 bar and equals 0.994. The adsorption of CO_2 in UiO-66 decreases ca. 1.3 times withing the temperature range from 298.15 to 800 K, and also decreases with increasing pressure by ca. 1.02 times in the range from 1 to 60 bar. The adsorptions of CO_2 and H_2 are inversely related: as the mole fraction of CO_2 decreases, more H_2 is adsorbed. The adsorption of H_2 in UiO-66 increases ca. 35 times withing the temperature range from 298.15 to 800 K and ca. 1.4 times withing the pressure range from 1 to 60 bar. The highest mole fraction of H_2 is obtained at 800 K and 60 bar and equals 0.27. The increasing temperature strengthens the interactions between the framework and H_2. The adsorption of H_2 is favored by UiO-66 with increasing temperature, resulting in the decrease of mole fractions of CO_2 and HCOOH. The amount of adsorbed reagents in UiO-66 varies, and the production of HCOOH is limited to the least adsorbed compound (H_2), due to the stoichiometry of the CO_2 hydrogenation reaction. The adsorption of H_2 increases with pressure, resulting in an increase in the production of HCOOH. Despite the increased adsorption of H_2 with temperature, the production of HCOOH decreases, which suggests that the interaction of HCOOH with the adsorbent becomes weaker.

To understand the reason for the decrease of mole fractions of HCOOH with increasing temperature and the increase of mole fractions of H_2, the infinite dilution was assumed and the isosteric heat of adsorption was computed at 298.15–800 K. In Fig. 6, the isosteric heat of adsorption for CO_2, H_2 and HCOOH is shown, that is a measure of the change of enthalpy when adsorbate molecules are adsorbed from the bulk-phase to the adsorbed phase. The adsorbate molecules are at a lower energy state on the adsorbent surface than in the bulk-phase, causing the liberation of heat. The enthalpy of adsorption of HCOOH noticeably decrease by 2.7 kJ mol^{-1} in the temperature range from 298.15 to 400 K. The increase in temperature leads to higher energy state of HCOOH on the adsorbent surface. The interactions between the host (UiO-66) and guest (HCOOH) become weaker, resulting in less heat released. This behavior is reflected in the decreasing production of HCOOH with increasing temperature in Fig. 4. The increase of temperature causes the decrease in the enthalpy of adsorption of CO_2 by 0.5 kJ mol^{-1} in the temperature range from 298.15 to 400 K. However, in the temperature range from 600 to 800 K, the slight increase by 0.4 kJ mol^{-1} is observed. The enthalpy of adsorption of H_2 increases by 3 kJ mol^{-1} with temperature in the range from 298.15 to 800 K. The linear behavior of the heat of adsorption at increasing temperature results from the fact that the increment of RT is larger than the variation of the hydrogen adsorption energy ΔU inside the
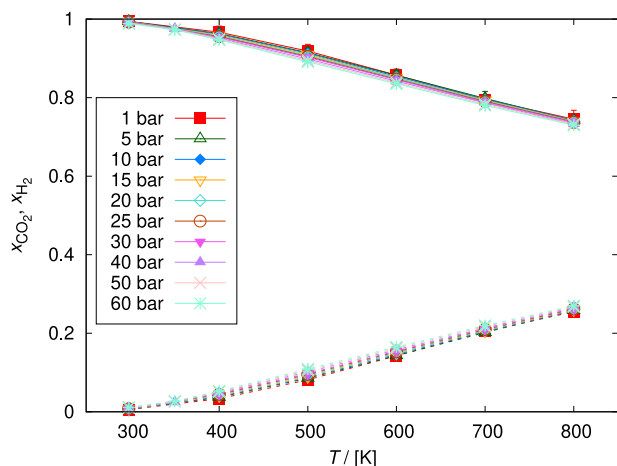
Fig. 5. CO_2 and H_2 mole fractions computed from GCMC simulations in UiO-66 framework. The data points of CO_2 mole fractions are connected to guide the eye by the solid lines and the data points of H_2 mole fractions by the dashed lines. The mole fractions of CO_2 and H_2 computed from the Rx/CFC simulations are used as an input for GCMC ensemble. The simulations were carried out at 298.15–800 K and 1–60 bar. The mole fractions of CO_2 decrease with increasing pressure and temperature. The mole fractions of H_2 increase with pressure and temperature.
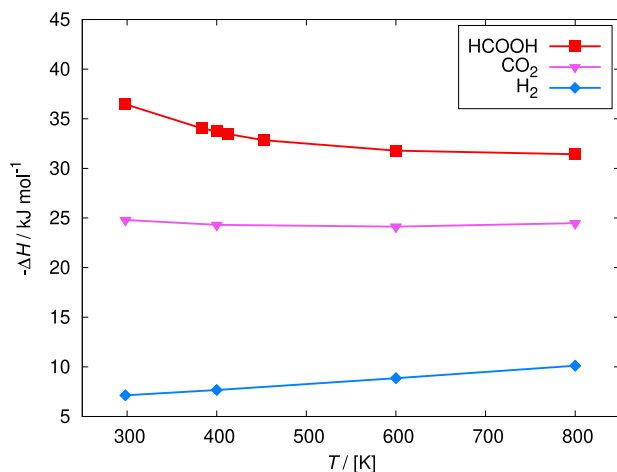

Fig. 6. Isosteric heat of adsorption of CO_2, H_2 and HCOOH at 298.15–800 K in UiO-66. The isosteric heat of adsorption of HCOOH decreases in the temperature range from 298.15 to 400 K. The energy state of HCOOH on the adsorbent surface increases, leading to weaker interactions between the framework and adsorbate. The increase of temperature causes the decrease in the enthalpy of adsorption of CO_2 in the temperature range from 298.15 to 400 K. The opposite effect is in the case of H_2, which enthalpy of adsorption increases with temperature in the range from 298.15 to 800 K. The error bars are smaller than the size of the symbols.

host-framework (see Table S7 of the Supporting Information) according to $-\Delta H = -(\Delta U - RT) = RT - \Delta U$. This behavior has been previously reported by Martín-Calvo et al. [118]. These authors showed that above 200 K, the heat of adsorption of hydrogen in all the zeolites linearly increases as a function of temperature. In this work, we also observe that despite differences between pore sizes, the trend and the obtained values of heat of adsorption of H_2 are similar for all three MOFs.

The distribution of CO_2, H_2 and HCOOH molecules at 298.15 K, 60 bar can be analyzed inside UiO-66 with the average density profiles (Fig. 7). The center of mass of the molecules that are adsorbed was projected onto the XY plane, which is the same as YZ and ZX planes in isotropic UiO-66. Fig. 7a is a reference structure of the UiO-66 framework. The average density profiles of HCOOH in Fig. 7b in UiO-66 show a very low adsorption loading compared to CO_2 ($x_{HCOOH} = 1.5$

Table 2

Enhancement (*ENH*, Eq. (8)) in the production of HCOOH obtained from GCMC simulations in UiO-66, Cu-BTC, and IRMOF-1 frameworks at 298.15–800 K and 1–60 bar. The HCOOH mole fractions computed from Rx/CFC simulations are used as an input for GCMC ensemble. The enhancement in HCOOH production resulting from the effect of confinement decreases with increasing temperature. The enhancement in the HCOOH production is the highest in Cu-BTC framework. The subscripts show uncertainties computed using error propagation rules. The enhancement value obtained in UiO-66 at 800 K and 1 bar was rejected due to high uncertainty.

| P/[bar]	T/[K]	ENH_{UiO-66}	ENH_{Cu-BTC}	$ENH_{IRMOF-1}$
1	298.15	$127.5_{180.9}$	$668.9_{635.3}$	$3.6_{7.3}$
	400	$0.8_{1.7}$	$8.2_{8.8}$	0_0
	500	$10.0_{27.8}$	$12.4_{15.0}$	0_0
	600	0_0	0_0	0_0
	700	0_0	0_0	0_0
	800	0_0	0_0	0_0
5	298.15	$181.9_{82.5}$	$1514.3_{509.0}$	$46.0_{52.4}$
	400	$7.4_{7.7}$	$34.4_{10.1}$	$7.8_{10.4}$
	500	$2.9_{7.9}$	$17.9_{11.6}$	$2.9_{3.1}$
	600	$0.3_{0.8}$	$12.3_{5.2}$	$2.1_{2.7}$
	700	$6.2_{9.7}$	$1.9_{2.5}$	$1.2_{1.7}$
	800	$6.1_{11.8}$	$0.2_{0.4}$	$0.9_{1.8}$
10	298.15	$187.9_{99.1}$	$2748.3_{591.2}$	$38.5_{18.4}$
	400	$17.0_{14.2}$	$48.6_{10.8}$	$4.2_{3.1}$
	500	$12.9_{10.0}$	$14.7_{4.2}$	$3.2_{1.5}$
	600	$8.4_{10.1}$	$4.1_{1.8}$	$2.7_{1.1}$
	700	$4.5_{4.1}$	$4.6_{2.1}$	$1.3_{1.2}$
	800	$3.2_{4.9}$	$3.7_{1.5}$	$1.8_{0.9}$
15	298.15	$241.8_{54.0}$	$2750.8_{412.2}$	$43.1_{13.1}$
	400	$12.5_{10.3}$	$73.8_{23.6}$	$4.6_{1.2}$
	500	$7.8_{6.6}$	$12.2_{4.6}$	$3.1_{0.7}$
	600	$5.0_{4.5}$	$5.3_{1.7}$	$2.3_{0.6}$
	700	$4.0_{4.8}$	$3.7_{1.0}$	$1.8_{1.0}$
	800	$1.1_{1.4}$	$2.0_{1.0}$	$1.9_{0.5}$
20	298.15	$299.7_{257.2}$	$2460.5_{333.5}$	$44.3_{12.8}$
	400	$9.1_{5.3}$	$49.8_{5.1}$	$4.8_{1.2}$
	500	$7.5_{5.9}$	$12.7_{1.3}$	$2.1_{0.6}$
	600	$3.8_{2.0}$	$5.9_{2.8}$	$2.0_{0.7}$
	700	$3.4_{2.0}$	$3.7_{1.0}$	$2.1_{0.4}$
	800	$3.8_{1.8}$	$2.8_{0.5}$	$1.6_{0.3}$
25	298.15	$227.3_{83.3}$	$2543.1_{698.3}$	$62.2_{22.8}$
	400	$15.1_{8.6}$	$48.9_{8.2}$	$5.3_{1.4}$
	500	$6.1_{4.1}$	$10.4_{2.2}$	$3.0_{0.8}$
	600	$3.9_{2.4}$	$5.9_{0.6}$	$2.5_{0.5}$
	700	$2.9_{1.5}$	$4.2_{0.6}$	$2.1_{0.6}$
	800	$2.7_{3.1}$	$2.7_{0.3}$	$1.5_{0.4}$
30	298.15	$195.6_{133.4}$	$2461.4_{372.4}$	$72.2_{25.9}$
	400	$13.9_{4.5}$	$45.3_{9.9}$	$5.1_{0.9}$
	500	$6.3_{1.6}$	$11.0_{1.2}$	$3.6_{0.6}$
	600	$5.0_{2.8}$	$5.4_{0.8}$	$2.1_{0.2}$
	700	$2.8_{1.0}$	$3.8_{0.5}$	$1.5_{0.6}$
	800	$3.5_{0.7}$	$2.4_{0.5}$	$1.6_{0.5}$
40	298.15	$280.5_{53.5}$	$2415.7_{315.1}$	$86.1_{24.0}$
	350	$33.3_{15.6}$	$264.8_{30.3}$	$11.3_{2.4}$
	400	$10.9_{3.9}$	$52.4_{8.0}$	$5.9_{1.7}$
	500	$4.7_{2.0}$	$13.4_{1.5}$	$2.6_{0.4}$
	600	$4.3_{1.7}$	$4.8_{0.6}$	$2.1_{0.5}$
	700	$3.7_{0.7}$	$3.5_{0.2}$	$2.0_{0.3}$
	800	$2.7_{0.6}$	$2.6_{0.2}$	$1.6_{0.4}$
50	298.15	$202.0_{96.1}$	$2020.8_{631.6}$	$80.7_{36.4}$
	350	$33.4_{13.4}$	$249.1_{41.1}$	$12.3_{2.5}$
	400	$11.6_{3.4}$	$56.8_{3.9}$	$5.9_{0.9}$
	500	$4.9_{1.3}$	$11.9_{1.0}$	$2.8_{0.5}$
	600	$4.7_{1.8}$	$5.7_{0.9}$	$2.4_{0.3}$
	700	$3.6_{0.9}$	$3.6_{0.3}$	$2.0_{0.3}$
	800	$3.0_{0.8}$	$2.6_{0.3}$	$1.7_{0.2}$
60	298.15	$176.5_{73.9}$	$1819.3_{229.8}$	$66.6_{12.1}$
	350	$34.1_{8.2}$	$241.9_{17.1}$	$12.0_{1.9}$
	400	$11.9_{3.5}$	$55.2_{3.8}$	$6.0_{1.1}$
	500	$5.3_{1.5}$	$11.3_{0.8}$	$3.1_{0.4}$
	600	$4.8_{2.3}$	$5.3_{0.5}$	$2.4_{0.4}$
	700	$3.1_{0.4}$	$3.5_{0.5}$	$1.6_{0.1}$
	800	$2.9_{0.7}$	$2.7_{0.1}$	$1.8_{0.3}$

(a)

(b)

(c)

(d)
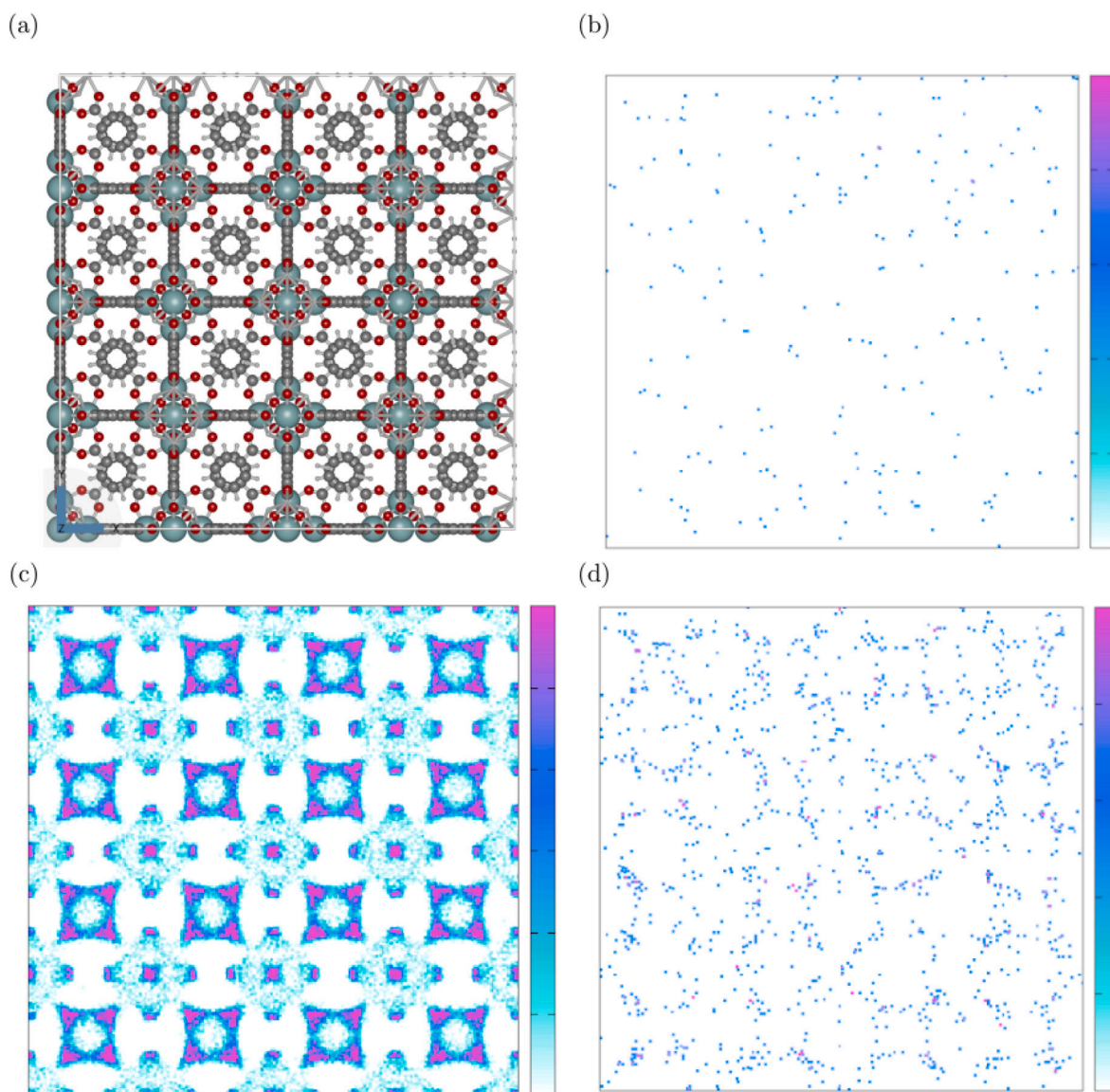
Fig. 7. The distribution of the HCOOH, CO₂ and H₂ molecules inside UiO-66, analyzed using density profiles from GCMC simulation at 298.15 K, 60 bar: (a) an atomistic reference structure of UiO-66 empty framework, visualized using iRASPA [119], (b) the distribution of HCOOH molecules ($x_{HCOOH} = 1.5 \cdot 10^{-4}$), (c) the distribution of CO₂ molecules (x_{CO_2} = 0.99), (d) the distribution of H₂ molecules (x_{H_2} = 0.01116). The center of mass of the molecules that are adsorbed was projected onto the XY plane. The projections onto YZ and ZX planes are identical due to the isotropy of UiO-66. The color gradation of the scales relates to the most and least populated regions of the structure, which is relative in each case. The preferential sites of CO₂ molecules (colored magenta) are surroundings of the zirconium centers and carbon hexagonal structures connected to the oxygen and hydrogen atoms. H₂ molecules are adsorbed surrounding the carbon hexagonal structure. The adsorption loading of HCOOH in UiO-66 is very low and the molecules of HCOOH tend to be located near carbon hexagonal structures and the zirconium centers, which are occupied by CO₂ molecules. The color scale is shown as a reference of the molecules loading.

$\cdot 10^{-4}$). HCOOH molecules tends to be located surrounding the carbon hexagonal structure connected to the oxygen and hydrogen atoms and near the zirconium centers. Fig. 7c and d show the distributions of CO₂ and H₂ molecules in the structure. CO₂ (x_{CO_2} = 0.99) is densely located surrounding the carbon hexagonal structure and near the zirconium centers. These positions in the pores have been filled, because CO₂ can form hydrogen bonds with H atoms belonging to the framework. The visualization of the CO₂ molecule interacting with H atom of the framework is shown in Figure S5 of the Supporting Information. The access of HCOOH molecules to their preferential sites is difficult due to the high loading of CO₂ molecules, competing for the same location. The amount of the H₂ molecules adsorbed is lower than for CO₂ (x_{H_2} = 0.01116), but preferential sites can be described as surrounding the carbon hexagonal structure.

The enhancement in HCOOH production resulting from the UiO-66 confinement was compared with the Cu-BTC and IRMOF-1 results. The mole fractions obtained from GCMC simulations in Cu-BTC and IRMOF-1 frameworks are listed in Tables S8 and S9 of the Supporting Information, respectively. The mole fractions of HCOOH are shown as a function of temperature and pressure in Figures S6 and S7 of the Supporting Information. The comparison of HCOOH mole fractions obtained in UiO-66, Cu-BTC, and IRMOF-1 at 60 bar is shown in Figure S8 of the Supporting Information. The mole fractions of HCOOH increase with pressure and decrease with the increasing temperature, due to the host-guest interactions becoming weaker (see isosteric heat of adsorption shown in Figures S9 and S10 of the Supporting Information). The calculated *ENH* results for UiO-66, Cu-BTC, and IRMOF-1 frameworks at 298.15–800 K and 1–60 bar are listed in Table 2.
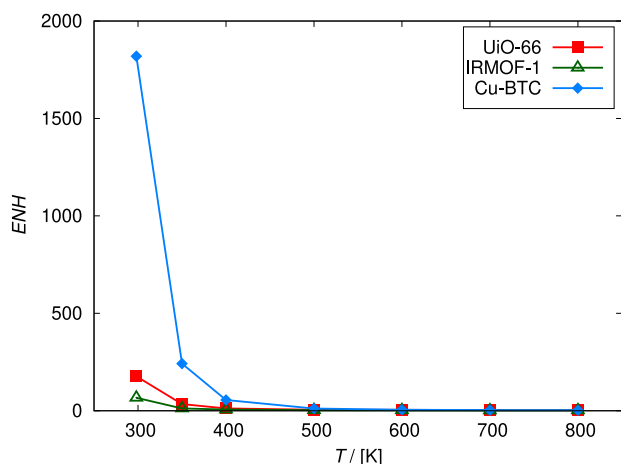
Fig. 8. Enhancement (*ENH*, Eq. (8)) in the production of HCOOH obtained from GCMC simulations in UiO-66, Cu-BTC, and IRMOF-1 frameworks at 298.15–800 K and 60 bar. The enhancement in HCOOH production resulting from the effect of confinement decreases with increasing temperature. The enhancement in the HCOOH production is the highest in Cu-BTC framework. The obtained mole fraction of HCOOH is 1819 times higher compared to the bulk-phase at 298.15 K.

The most efficient conditions for all the systems resulting in the highest mole fraction of HCOOH are at 298.15 K, 60 bar. The enhancement in the HCOOH production is the highest in Cu-BTC framework, see Fig. 8. The obtained mole fraction of HCOOH equals 0.0016 at 298.15 K, reaching a value 1819 times higher compared to the bulk-phase. A large discrepancy is noticeable between the enhancement in HCOOH production caused by Cu-BTC and the effect of UiO-66 (x_{HCOOH} is 176 times higher compared to the gas phase) and IRMOF-1 (x_{HCOOH} is 67 times higher compared to the gas phase). To assess if this difference is caused by the impact of different pore size or metal centers of the studied MOFs, the pore size distributions were compared in Figure S2 of the Supporting Information. There are two types of micropores with a diameter at 3.5 Å and 7 Å present in the UiO-66. Cu-BTC is characterized by larger micropores with diameters at 5, 11, and 13 Å. The diameters of micropores in IRMOF-1 are at 11, and 15 Å. UiO-66 causes the strongest confinement, although in Cu-BTC the production of HCOOH is ca. 10 times bigger than in UiO-66. The stronger confinement resulting from the smaller pore size is found to not improve the production of HCOOH in CO_2 hydrogenation reaction.

Radial distribution functions were computed to analyze the effect of metal centers on HCOOH adsorption in UiO-66, Cu-BTC, and IRMOF-1 at 298.15 K, see Figures S11–S13 of the Supporting Information. The preferential distance of the adsorbed molecules of HCOOH to the metal centers is the closest in Cu-BTC framework and equals to 2.4 Å. Simultaneously, the highest number of molecules (6) are noticeable in Cu-BTC within the preferential distance to the metal centers. This indicates a significant influence of the type of metal center on CO_2 hydrogenation reaction, exceeding the influence of the pore size in the structure. The application of Cu-BTC makes it possible to eliminate the high-cost temperature elevation, which is necessary in most of the analyzed cases to obtain a higher purity of the product.

In Table 3, the effect of confinement on the CO_2 hydrogenation using Cu-BTC at 298.15 K and 60 bar was compared with the performance of transition metal catalysts with phosphine ligands [26,29], pincer ligands [30], N-heterocyclic carbene ligands [27,34,35], and half-sandwich catalysts with proton-responsive ligands [36,37,39,40]. From each considered study, two types of catalysts were selected based on the highest and lowest concentration of the product of CO_2 hydrogenation. The final concentration of HCOOH obtained from the Cu-BTC confinement is ca. 80 times lower than the highest reported concentration

obtained with the use of the Wilkinson complex [26], and ca. 30 times higher than the lowest reported concentration obtained using a catalyst with N-heterocyclic carbene ligands [34]. The concentration of HCOOH obtained from the confinement effect is between the highest and lowest concentration of the product obtained with the use of transition metal catalysts. Despite the minor difference between the molecular form of HCOOH and the ionic form (formate), the dissociation state of the acid significantly affects the selection of a proper downstream separation process [17]. An economic analysis for formic acid/formate downstream processing methods has been performed by Ramdin et al. [17], which shows that HCOOH is more valuable as a product than formate. The processes of separation, concentration, and acidification of formate solutions are challenging. The conversion and concentration of 10 wt% formate to 85 wt% formic acid add around \$380/ton of FA to the total production costs [17]. The application of Cu-BTC has the potential to improve the economically more attractive direct method of CO_2 conversion through downstream separation cost reduction. Further studies of Cu-BTC toward its functionalization may be a promising subject of research in the field of CO_2 hydrogenation.

6. Conclusions

We carried out molecular simulations to study the performance of UiO-66 for the production process of formic acid, followed by comparison with the performance of Cu-BTC, and IRMOF-1. The effect of confinement on the yield of HCOOH from the CO_2 hydrogenation reaction was analyzed. The adsorption isobars of the studied systems were computed with Monte Carlo simulations in the grand-canonical ensemble. It was shown that the confinement increases the HCOOH production, due to the higher density of pore phase compared to the bulk-phase and the selective adsorption of HCOOH as a favored component, by Le Chatelier's principle. The HCOOH mole fractions increase with pressure and decrease with the increasing temperature. The most efficient conditions for the HCOOH production in the confinement are at 298.15 K and 60 bar. The production of HCOOH in UiO-66 framework is ca. 200 times higher compared to the gas phase. The most significant enhancement in HCOOH production (ca. 2000 times higher compared to the gas phase) is achieved using Cu-BTC, resulting in $x_{GCMC} = 0.0016$ from $x_{Rx/CFC} = 8.63 \cdot 10^{-7}$ at 298.15 K and 60 bar. The increase in temperature leads to the higher energy state of HCOOH on the adsorbent surface and weaker interactions between the framework and adsorbate, causing the decrease of enhancement. At 1 bar, HCOOH is obtained in UiO-66 and Cu-BTC up to 500 K and in IRMOF-1 only at 298.15 K. By comparing the performance of MOFs with different pore size distributions and metal centers, it is found that the stronger confinement resulting from the smaller pores does not guarantee the improvement of HCOOH production in CO_2 hydrogenation reaction. The prevailing factor is the type of metal center in the metal–organic framework. The highest number of HCOOH molecules in the closest distance to the metal center is located near the Cu center in Cu-BTC. The metal–organic framework Cu-BTC has the potential to be a useful alternative or supplement to transition metal catalysts for improving the efficiency of CO_2 hydrogenation due to: (a) elimination of the high-cost temperature elevation, (b) more valuable final product enabling cost reduction of downstream processing methods, and (c) comparable final concentration of HCOOH to the reported concentrations of formate obtained using transition metal catalysts. To fully investigate its performance, a techno-economic and carbon emission analysis should be conducted. An interesting topic for future research would be a kinetic study of the Cu-BTC catalytic performance in CO_2 hydrogenation and the functionalization of Cu-BTC structure to improve the adsorption of HCOOH. This would allow a better understanding of the CO_2 hydrogenation reaction to HCOOH in confinement.

Table 3

CO_2 hydrogenation using transition metal catalysts. The final concentration of HCOOH obtained in this work using Cu-BTC at 298.15 K and 60 bar was ca. 80 times lower than the highest reported concentration obtained with the use of Wilkinson complex [26], and ca. 30 times higher than the lowest reported concentration obtained using a catalyst with N-heterocyclic carbene ligands [34]. The final concentration of HCOOH in the adsorbed phase was calculated as $c_{HCOOH} = \frac{n_{HCOOH}}{(\xi \cdot V)}$, where n_{HCOOH} is the number of moles of HCOOH adsorbed in a unit cell, V is the volume of the unit cell, and ξ is the helium void fraction.

Catalyst	Conditions	Product	Concentration /[mol L^{-1}]	Reference
None	Cu-BTC confinement, 298.15 K, 60 bar	HCOOH	0.031	this work
4DHBP Ir(III) complex no. 1	298.15 K, 1 bar, 24 h	formate	0.005	[40]
4DHBP Ir(III) complex no. 4	353.15 K, 30 bar 8 h	formate	0.687	[40]
[Cp*Ir(6,6'-R$_2$-bpy)(OH$_2$)]SO$_4$ (R=OMe)	353.15 K, 10 bar, 8 h	formate	0.004	[39]
Cp*Ir, thbpym ligand	323.15 K, 10 bar, 8 h	formate	0.480	[39]
Ir(III) complex [3(OH$_2$)$_2$]$^{4+}$	323.15 K, 10 bar, 2 h	formate	0.006	[37]
Ir(III) complex 2'(OH$_2$)$_2$	323.15 K, 30 bar, 48 h	formate	1.7	[37]
[RhCl(η^4 C$_8$H$_1$2)]$_2$	298.15 K, 40 bar, 22 h	formate	1.55	[27]
Ir(PNP), pincer ligand	473.15 K, 50 bar, 2 h	formate	0.6	[30]
Cp*Ir(III) complex no. 5	303.15 K, 1 bar, 30 h	formate	0.016	[36]
(C$_6$Me$_6$)*Ru(II) complex no. 6	393.15 K, 60 bar, 24 h	formate	1.54	[36]
Cp*Rh(III) complex no. 4	353.15 K, 40 bar, 32 h	formate	0.24	[36]
[Ir(bis-NHC)(AcO)I$_2$] complex no. 1, N-heterocyclic carbene ligand	353.15 K, 60 bar, 20 h	formate	0.01	[35]
[Ir(bis-NHC)(AcO)I$_2$] complex no. 3, N-heterocyclic carbene ligand	473.15 K, 60 bar, 75 h	formate	0.38	[35]
(η^6-arene)Ru(bis-NHC) complex no. 1	353.15 K, 40 bar, 1 h	formate	0.001	[34]
(η^6-arene)Ru(bis-NHC) complex no. 1	473.15 K, 40 bar, 20 h	formate	0.13	[34]
[RhCl(mtppms)$_3$]	323.15 K, 60 bar, 24 h, CaCO$_3$	HCOOH	0.01	[29]
[RhCl(mtppms)$_3$]	323.15 K, 100 bar, 20 h, HCOONa	HCOOH	0.12	[29]
Rh(acac)(CO)$_2$, Dppe ligand	298.15 K, p_{CO_2} = 40 bar, p_{H_2} = 20 bar, 20 h	HCOOH·NEt$_3$	0.03	[26]
Wilkinson complex RhCl(PPh$_3$)$_3$ + 3 PPh$_3$	298.15 K, p_{CO_2} = 40 bar, p_{H_2} = 20 bar, 20 h	HCOOH	2.50	[26]

Declaration of competing interest

The authors declare that they have no known competing financial interests or personal relationships that could have appeared to influence the work reported in this paper.

Data availability

Data will be made available on request.

Appendix A. Supplementary data

The following is available free of charge:

- Information about the ideal-gas partition functions of CO_2, H_2, and HCOOH at 298.15–800 K;
- The validation of ideal-gas partition functions — the equilibrium composition of syngas obtained by cofeeding HCOOH to the steam reforming of methane reaction at 1 bar, $H_2O:CH_4$ = 1 and HCOOH:H_2O = 0.5;
- Geometries for the CO_2, H_2, and HCOOH models;
- Cell parameters for UiO-66, Cu-BTC, and IRMOF-1;
- Mole fractions of CO_2, H_2, and HCOOH obtained from Continuous Fractional Component Monte Carlo simulations in the Reaction Ensemble at 298.15–800 K, and 1–60 bar;
- Fugacity coefficients of CO_2, H_2, and HCOOH computed using the Peng-Robinson equation of state at 298.15–800 K, and 1–60 bar;
- Mole fractions of CO_2, H_2, and HCOOH obtained from grand-canonical Monte Carlo simulations at 298.15–800 K, and 1–60 bar;
- Enthalpy of adsorption at infinite dilution of CO_2, H_2, and HCOOH in Cu-BTC, and IRMOF-1;
- Radial distribution functions for HCOOH and metal centers in UiO-66, Cu-BTC, and IRMOF-1.

Supplementary material related to this article can be found online at https://doi.org/10.1016/j.cej.2023.143432.

References

[1] F. Joos, R. Spahni, Rates of change in natural and anthropogenic radiative forcing over the past 20,000 years, Proc. Natl. Acad. Sci. 105 (2008) 1425–1430.

[2] E. Dlugokencky, P. Tans, Trends in Atmospheric Carbon Dioxide, National Oceanic and Atmospheric Administration, Earth System Research Laboratory (NOAA/ESRL, 2022, http://www.esrl.noaa.gov/gmd/ccgg/trends/global.html (Access date: 11 March 2022).

[3] S.C. Peter, Reduction of CO_2 to chemicals and fuels: A solution to global warming and energy crisis, ACS Energy Lett. 3 (2018) 1557–1561.

[4] N.M. Dowell, P.S. Fennell, N. Shah, G.C. Maitland, The role of CO_2 capture and utilization in mitigating climate change, Nature Clim. Change 7 (2017) 243–249.

[5] N.B. Singh, in: H. Pöllmann (Ed.), In Conversion of CO_2 Into Useful Products. Industrial Waste: Characterization, Modification and Applications of Residues, fourth ed., De Gruyter, Berlin, Boston, 2021, pp. 319–344.

[6] M. Aresta (Ed.), Carbon Dioxide Recovery and Utilization, fourth ed., Kluwer Academic Publishers, Dordrecht, 2010.

[7] M. Grasemann, G. Laurenczy, Formic acid as a hydrogen source – recent developments and future trends, Energy Environ. Sci. 5 (2012) 8171–8181.

[8] D. Adams, R. Boopathy, Use of formic acid to control vibriosis in shrimp aquaculture, Biologia 68 (2013) 1017–1021.

[9] N.P. Cheremisinoff, P.E. Rosenfeld, Chapter 6 - sources of air emissions from pulp and paper mills, in: Handbook of Pollution Prevention and Cleaner Production, William Andrew Publishing, Oxford, 2010, pp. 179–259.

[10] N. Fathima, J. Rao, B. Nair, Cost effective fixing process for post tanning operation, Jalca 105 (2010) 100–106.

[11] J. Hietala, A. Vuori, P. Johnsson, I. Pollari, W. Reutemann, H. Kieczka, Formic acid, in: Ullmann's Encyclopedia of Industrial Chemistry, John Wiley & Sons, Ltd, 2016, pp. 1–22.

[12] Y. Yasaka, K. Yoshida, C. Wakai, N. Matubayasi, M. Nakahara, Kinetic and equilibrium study on formic acid decomposition in relation to the water-gas-shift reaction, J. Phys. Chem. A. 110 (2006) 11082.

[13] Fact.MR, Formic acid market analysis by concentration (formic acid of 85% concentration, 90% concentration, 94% concentration, 99% concentration), by application (formic acid for animal feed, agricultural products, leather tanning), by region - global insights 2021–2031, 2021, URL https://www.factmr.com/report/4279/formic-acid-market (Access date: 20 August 2022).

[14] H. Yang, J.J. Kaczur, S.D. Sajjad, R.I. Masel, Electrochemical conversion of CO_2 to formic acid utilizing sustainion^{TM} membranes, J. CO_2 Util. 20 (2017) 208–217.

[15] X. Lu, D.Y.C. Leung, H. Wang, M.K.H. Leung, J. Xuan, Electrochemical reduction of carbon dioxide to formic acid, ChemElectroChem 1 (5) (2014) 836–849.

[16] B. Hu, C. Guild, S.L. Suib, Thermal, electrochemical, and photochemical conversion of CO_2 to fuels and value-added products, J. CO_2 Util. 1 (2013) 18–27.

[17] M. Ramdin, A.R.T. Morrison, M. de Groen, R. van Haperen, R. de Kler, E. Irtem, A.T. Laitinen, L.J.P. van den Broeke, T. Breugelmans, J.P.M. Trusler, W.d. Jong, T.J.H. Vlugt, High-pressure electrochemical reduction of CO2 to formic acid/formate: Effect of pH on the downstream separation process and economics, Ind. Eng. Chem. Res. 58 (51) (2019) 22718–22740.

[18] D.O. Wasik, H.M. Polat, M. Ramdin, O.A. Moultos, S. Calero, T.J.H. Vlugt, Solubility of CO_2 in aqueous formic acid solutions and the effect of NaCl addition: A molecular simulation study, J. Phys. Chem. C 126 (45) (2022) 19424–19434.

[19] M. König, J. Vaes, E. Klemm, D. Pant, Solvents and supporting electrolytes in the electrocatalytic reduction of CO_2, IScience 19 (2019) 135–160.

[20] M. Duarte, B. De Mot, J. Hereijgers, T. Breugelmans, Electrochemical reduction of CO_2: Effect of convective CO_2 supply in gas diffusion electrodes, ChemElectroChem 6 (22) (2019) 5596–5602.

[21] B. De Mot, J. Hereijgers, M. Duarte, T. Breugelmans, Influence of flow and pressure distribution inside a gas diffusion electrode on the performance of a flow-by CO_2 electrolyzer, Chem. Eng. J. 378 (2019) 122224.

[22] B. De Mot, M. Ramdin, J. Hereijgers, T.J.H. Vlugt, T. Breugelmans, Direct water injection in catholyte-free zero-gap carbon dioxide electrolyzers, ChemElectroChem 7 (18) (2020) 3839–3843.

[23] S. Moret, P.J. Dyson, G. Laurenczy, Direct synthesis of formic acid from carbon dioxide by hydrogenation in acidic media, Nature Commun. 5 (2014) 4017.

[24] M. Ghara, P.K. Chattaraj, A computational study on hydrogenation of CO_2, catalyzed by a bridged B/N frustrated Lewis pair, Struct. Chem. 30 (2019) 1067–1077.

[25] Y. Inoue, H. Izumida, Y. Sasaki, H. Hashimoto, Catalytic fixation of carbon dioxide to formic acid by transition-metal complexes under mild conditions, Chem. Lett. 5 (1976) 863–864.

[26] N.N. Ezhova, N.V. Kolesnichenko, A.V. Bulygin, E.V. Slivinskii, S. Han, Hydrogenation of CO_2 to formic acid in the presence of the Wilkinson complex, Russ. Chem. Bull. Int. Ed 51 (2002) 2165–2169.

[27] E. Graf, W. Leitner, Direct formation of formic acid from carbon dioxide and dihydrogen using the $[(Rh(Cod)Cl)_2]Ph_2P(CH_2)_4PPh_2$ catalyst system, J. Chem. Soc. Chem. Commun. (1992) 623–624.

[28] F. Gassner, W. Leitner, Hydrogenation of carbon dioxide to formic acid using water-soluble rhodium catalysts, J. Chem. Soc. Chem. Commun. (1993) 1465–1466.

[29] G. Zhao, F. Joó, Free formic acid by hydrogenation of carbon dioxide in sodium formate solutions, Catal. Commun. 14 (2011) 74–76.

[30] R. Tanaka, M. Yamashita, K. Nozaki, Catalytic hydrogenation of carbon dioxide using Ir(III)-Pincer complexes, J. Am. Chem. Soc. 131 (40) (2009) 14168–14169.

[31] R. Tanaka, M. Yamashita, L.W. Chung, K. Morokuma, K. Nozaki, Mechanistic studies on the reversible hydrogenation of carbon dioxide catalyzed by an Ir-PNP complex, Organometallics 30 (24) (2011) 6742–6750.

[32] T.J. Schmeier, G.E. Dobereiner, R.H. Crabtree, N. Hazari, Secondary coordination sphere interactions facilitate the insertion step in an Iridium(III) CO_2 reduction catalyst, J. Am. Chem. Soc. 133 (24) (2011) 9274–9277.

[33] S. Sanz, M. Benítez, E. Peris, A new approach to the reduction of carbon dioxide: CO_2 reduction to formate by transfer hydrogenation in iPrOH, Organometallics 29 (1) (2010) 275–277.

[34] S. Sanz, A. Azua, E. Peris, '(η^6-Arene)Ru(bis-NHC)' complexes for the reduction of CO_2 to formate with hydrogen and by transfer hydrogenation with *i*PrOH, Dalton Trans. 39 (2010) 6339–6343.

[35] A. Azua, S. Sanz, E. Peris, Water-soluble Ir^{III} N-heterocyclic carbene based catalysts for the reduction of CO_2 to formate by transfer hydrogenation and the deuteration of aryl amines in water, Chem. – A Eur. J. 17 (14) (2011) 3963–3967.

[36] Y. Himeda, N. Onozawa-Komatsuzaki, H. Sugihara, K. Kasuga, Simultaneous tuning of activity and water solubility of complex catalysts by acid - base equilibrium of ligands for conversion of carbon dioxide, Organometallics 26 (3) (2007) 702–712.

[37] J.F. Hull, Y. Himeda, W.-H. Wang, B. Hashiguchi, R. Periana, D.J. Szalda, J.T. Muckerman, E. Fujita, Reversible hydrogen storage using CO_2 and a proton-switchable iridium catalyst in aqueous media under mild temperatures and pressures, Nature Chem. 4 (5) (2012) 383—388.

[38] Y. Suna, M.Z. Ertem, W.-H. Wang, H. Kambayashi, Y. Manaka, J.T. Muckerman, E. Fujita, Y. Himeda, Positional effects of hydroxy groups on catalytic activity of proton-responsive half-sandwich Cp*Iridium(III) complexes, Organometallics 33 (22) (2014) 6519–6530.

[39] W.-H. Wang, J.F. Hull, J.T. Muckerman, E. Fujita, Y. Himeda, Second-coordination-sphere and electronic effects enhance iridium(III)-catalyzed homogeneous hydrogenation of carbon dioxide in water near ambient temperature and pressure, Energy Environ. Sci. 5 (2012) 7923–7926.

[40] W.-H. Wang, J.T. Muckerman, E. Fujita, Y. Himeda, Mechanistic insight through factors controlling effective hydrogenation of CO_2 catalyzed by bioinspired proton-responsive Iridium(III) complexes, ACS Catal. 3 (5) (2013) 856–860.

[41] C. Mömming, E. Otten, G. Kehr, R. Fröhlich, S. Grimme, D. Stephan, G. Erker, Reversible metal-free carbon dioxide binding by frustrated Lewis Pairs, Angew. Chemie Int. Ed. 48 (36) (2009) 6643–6646.

[42] A.E. Ashley, A.L. Thompson, D. O'Hare, Non-metal-mediated homogeneous hydrogenation of CO_2 to CH_3OH, Angew. Chemie Int. Ed. 48 (52) (2009) 9839–9843.

[43] T. Zhao, X. Hu, Y. Wu, Z. Zhang, Hydrogenation of CO_2 to formate with H_2: Transition metal free catalyst based on a Lewis pair, Angew. Chemie Int. Ed. 58 (3) (2019) 722–726.

[44] H. Chatelier, O. Boudouard, On the flammable limits of gas mixtures, Process Saf. Progr. - PROCESS SAF PROG 24 (2005) 3–5.

[45] C.H. Turner, J.K. Johnson, K.E. Gubbins, Effect of confinement on chemical reaction equilibria: The reactions $2NO \rightleftarrows NO_2$ and $N_2+3H_2 \rightleftarrows NH_3$ in carbon micropores, J. Chem. Phys. 114 (4) (2001) 1851–1859.

[46] I. Matito-Martos, A. García-Reyes, A. Martin-Calvo, D. Dubbeldam, S. Calero, Improving ammonia production using zeolites, J. Phys. Chem. C 123 (30) (2019) 18475–18481.

[47] A. Trokhymchuk, O. Pizio, S. Sokołowski, Solvation force for an associative fluid in a slit-like pore, J. Colloid Interface Sci. 178 (2) (1996) 436–441.

[48] A. Trokhymchuk, D. Henderson, S. Sokołowski, Structure of chemically reacting particles near a hard wall from integral equations and computer simulations, Can. J. Phys. 74 (1–2) (1996) 65–76.

[49] O. Pizio, D. Henderson, S. Sokołowski, Density profiles of chemically reacting simple fluids near impenetrable surfaces, J. Phys. Chem. 99 (1995) 2408–2411.

[50] O. Pizio, D. Henderson, S. Sokołowski, Adsorption of chemically reacting fluids on a crystalline surface, Mol. Phys. 85 (2) (1995) 407–412.

[51] E.A. Müller, L.F. Vega, K.E. Gubbins, L.F. Rull, Adsorption isotherms of associating chain molecules from Monte Carlo simulations, Mol. Phys. 85 (1) (1995) 9–21.

[52] H.R. Abid, H. Tian, H.-M. Ang, M.O. Tade, C.E. Buckley, S. Wang, Nanosize Zr-metal organic framework (UiO-66) for hydrogen and carbon dioxide storage, Chem. Eng. J. 187 (2012) 415–420.

[53] X. Liu, L. Zhang, J. Wang, Design strategies for MOF-derived porous functional materials: Preserving surfaces and nurturing pores, J. Materiomics 7 (3) (2021) 440–459.

[54] Q. Gu, H.Y. Ng, D. Zhao, J. Wang, Metal–organic frameworks (MOFs)-boosted filtration membrane technology for water sustainability, APL Mater. 8 (4) (2020) 040902.

[55] Z. Wang, X. Xu, J. Kim, V. Malgras, R. Mo, C. Li, Y. Lin, H. Tan, J. Tang, L. Pan, Y. Bando, T. Yang, Y. Yamauchi, Nanoarchitectured metal–organic framework/polypyrrole hybrids for brackish water desalination using capacitive deionization, Mater. Horiz. 6 (2019) 1433–1437.

[56] N.L. Rosi, J. Eckert, M. Eddaoudi, D.T. Vodak, J. Kim, M. O'Keeffe, O.M. Yaghi, Hydrogen storage in microporous metal-organic frameworks, Science 300 (5622) (2003) 1127–1129.

[57] G. Férey, C. Mellot-Draznieks, C. Serre, F. Millange, J. Dutour, S. Surblé, I. Margiolaki, A chromium terephthalate-based solid with unusually large pore volumes and surface area, Science 309 (5743) (2005) 2040–2042.

[58] F.X. Llabrés i Xamena, A. Abad, A. Corma, H. Garcia, MOFs as catalysts: Activity, reusability and shape-selectivity of a Pd-containing MOF, J. Cataly. 250 (2) (2007) 294–298.

[59] L. Alaerts, E. Séguin, H. Poelman, F. Thibault-Starzyk, P.A. Jacobs, D.E.D. Vos, Probing the lewis acidity and catalytic activity of the metal–organic framework [Cu$_3$(btc)$_2$] (btc=benzene-1,3,5-tricarboxylate), Chem. – A Eur. J. 12 (28) (2006) 7353–7363.

[60] B. Gómez-Lor, E. Gutiérrez-Puebla, M. Iglesias, M.A. Monge, C. Ruiz-Valero, N. Snejko, Novel 2D and 3D indium metal-organic frameworks: Topology and catalytic properties, Chem. Mater. 17 (10) (2005) 2568–2573.

[61] Y.M.A. Yamada, Y. Maeda, Y. Uozumi, Novel 3D coordination palladium-network complex: A recyclable catalyst for Suzuki - Miyaura reaction, Org. Lett. 8 (19) (2006) 4259–4262.

[62] S.L. James, Metal-organic frameworks, Chem. Soc. Rev. 32 (2003) 276–288.

[63] J.L. Ong, A.C.M. Loy, S.Y. Teng, B.S. How, Future paradigm of 3D printed Ni-based metal organic framework catalysts for dry methane reforming: Techno-economic and environmental analyses, ACS Omega 7 (18) (2022) 15369–15384.

[64] J. Ye, J.K. Johnson, Design of Lewis pair-functionalized metal organic frameworks for CO$_2$ hydrogenation, ACS Catal. 5 (5) (2015) 2921–2928.

[65] J. Winarta, B. Shan, S.M. Mcintyre, L. Ye, C. Wang, J. Liu, B. Mu, A decade of UiO-66 research: A historic review of dynamic structure, synthesis mechanisms, and characterization techniques of an archetypal metal–organic framework, Cryst. Growth Des. 20 (2) (2020) 1347–1362.

[66] S.E. Bambalaza, H.W. Langmi, R. Mokaya, N.M. Musyoka, J. Ren, L.E. Khotseng, Compaction of a zirconium metal–organic framework (UiO-66) for high density hydrogen storage applications, J. Mater. Chem. A 6 (2018) 23569–23577.

[67] Q. Yang, A.D. Wiersum, P.L. Llewellyn, V. Guillerm, C. Serre, G. Maurin, Functionalizing porous zirconium terephthalate UiO-66(Zr) for natural gas upgrading: A computational exploration, Chem. Commun. 47 (2011) 9603–9605.

[68] H.R. Abid, G.H. Pham, H.-M. Ang, M.O. Tade, S. Wang, Adsorption of CH$_4$ and CO$_2$ on Zr-metal organic frameworks, J. Colloid Interface Sci. 366 (1) (2012) 120–124.

[69] J. Ye, J.K. Johnson, Screening lewis pair moieties for catalytic hydrogenation of CO$_2$ in functionalized UiO-66, ACS Catal. 5 (10) (2015) 6219–6229.

[70] K. Yang, J. Jiang, Computational design of a metal-based frustrated Lewis pair on defective UiO-66 for CO$_2$ hydrogenation to methanol, J. Mater. Chem. A 8 (2020) 22802–22815.

[71] A. Rahbari, M. Ramdin, L.J.P. van den Broeke, T.J.H. Vlugt, Combined steam reforming of methane and formic acid to produce syngas with an adjustable H$_2$:CO ratio, Ind. Eng. Chem. Res. 57 (31) (2018) 10663–10674.

[72] W. Shi, E.J. Maginn, Continuous fractional component Monte Carlo: An adaptive biasing method for open system atomistic simulations, J. Chem. Theory Comput. 3 (4) (2007) 1451–1463.

[73] W. Shi, E.J. Maginn, Improvement in molecule exchange efficiency in Gibbs ensemble Monte Carlo: Development and implementation of the continuous fractional component move, J. Comput. Chem. 29 (15) (2008) 2520–2530.

[74] A. Rahbari, R. Hens, M. Ramdin, O.A. Moultos, D. Dubbeldam, T.J.H. Vlugt, Recent advances in the continuous fractional component Monte Carlo methodology, Mol. Simul. 47 (10–11) (2021) 804–823.

[75] W.R. Smith, B. Triska, The reaction ensemble method for the computer simulation of chemical and phase equilibria. I. Theory and basic examples, J. Chem. Phys. 100 (4) (1994) 3019–3027.

[76] J.K. Johnson, A.Z. Panagiotopoulos, K.E. Gubbins, Reactive canonical Monte Carlo, Mol. Phys. 81 (3) (1994) 717–733.

[77] A. Poursaeidesfahani, R. Hens, A. Rahbari, M. Ramdin, D. Dubbeldam, T.J.H. Vlugt, Efficient application of continuous fractional component Monte Carlo in the reaction ensemble, J. Chem. Theory Comput. 13 (9) (2017) 4452–4466.

[78] R. Hens, A. Rahbari, S. Caro-Ortiz, N. Dawass, M. Erdős, A. Poursaeidesfahani, H.S. Salehi, A.T. Celebi, M. Ramdin, O.A. Moultos, D. Dubbeldam, T.J.H. Vlugt, Brick-CFCMC: Open source software for Monte Carlo simulations of phase and reaction equilibria using the continuous fractional component method, J. Chem. Inform. Model. 60 (6) (2020) 2678–2682.

[79] H.M. Polat, H.S. Salehi, R. Hens, D.O. Wasik, A. Rahbari, F. de Meyer, C. Houriez, C. Coquelet, S. Calero, D. Dubbeldam, O.A. Moultos, T.J.H. Vlugt, New features of the open source Monte Carlo software brick-CFCMC: Thermodynamic integration and hybrid trial moves, J. Chem. Inform. Model. 61 (8) (2021) 3752–3757.

[80] D. Dubbeldam, S. Calero, D.E. Ellis, R.Q. Snurr, RASPA: Molecular simulation software for adsorption and diffusion in flexible nanoporous materials, Mol. Simul. 42 (2) (2016) 81–101.

[81] D. Dubbeldam, A. Torres-Knoop, K.S. Walton, On the inner workings of Monte Carlo codes, Mol. Simul. 39 (14–15) (2013) 1253–1292.

[82] T.W. Rosch, E.J. Maginn, Reaction ensemble Monte Carlo simulation of complex molecular systems, J. Chem. Theory Comput. 7 (2) (2011) 269–279.

[83] C.H. Turner, J.K. Brennan, M. Lísal, W.R. Smith, J.K. Johnson, K.E. Gubbins, Simulation of chemical reaction equilibria by the reaction ensemble Monte Carlo method: A review, Mol. Simul. 34 (2) (2008) 119–146.

[84] C.H. Turner, J. Pikunic, K.E. Gubbins, Influence of chemical and physical surface heterogeneity on chemical reaction equilibria in carbon micropores, Mol. Phys. 99 (24) (2001) 1991–2001.

[85] M. Borówko, A. Patrykiejew, S. Sokołowski, R. Zagórski, O. Pizio, Chemical reactions at surfaces: Application of the reaction ensemble Monte Carlo method, Czech. J. Phys. 48 (3) (1998) 371–388.

[86] N. Hansen, S. Jakobtorweihen, F.J. Keil, Reactive Monte Carlo and grand-canonical Monte Carlo simulations of the propene metathesis reaction system, J. Chem. Phys. 122 (16) (2005) 164705.

[87] M. Lísal, J.K. Brennan, W.R. Smith, Chemical reaction equilibrium in nanoporous materials: NO dimerization reaction in carbon slit nanopores, J. Chem. Phys. 124 (6) (2006) 064712.

[88] A. Torres-Knoop, A. Poursaeidesfahani, T.J.H. Vlugt, D. Dubbeldam, Behavior of the enthalpy of adsorption in nanoporous materials close to saturation conditions, J. Chem. Theory Comput. 13 (7) (2017) 3326–3339.

[89] S.P. Balaji, S. Gangarapu, M. Ramdin, A. Torres-Knoop, H. Zuilhof, E.L.V. Goetheer, D. Dubbeldam, T.J.H. Vlugt, Simulating the reactions of CO$_2$ in aqueous monoethanolamine solution by reaction ensemble Monte Carlo using the continuous fractional component method, J. Chem. Theory Comput. 11 (6) (2015) 2661–2669.

[90] T. Shimanouchi, Tables of Molecular Vibrational Frequencies Consolidated Volume I, National Bureau of Standards, 1972, pp. 1–160.

[91] P.R. Davies, W.J. Orville-Thomas, Infrared band intensities and bond polarities, J. Mol. Struct. 4 (1969) 163–177.

[92] W.B. Person, G. Zerbi, Vibrational Intensities in Infrared and Raman Spectroscopy, Elsevier, Amsterdam, 1982.

[93] G. Herzberg, Electronic Spectra and Electronic Structure of Polyatomic Molecules, Van Nostrand, New York, 1966.

[94] K.P. Huber, G. Herzberg, Constants of diatomic molecules, in: Molecular Spectra and Molecular Structure: IV. Constants of Diatomic Molecules, Springer US, Boston, MA, 1979, pp. 8–689.

[95] D.A. McQuarrie, J.D. Simon, Physical Chemistry: A Molecular Approach, first ed., University Science Books, Sausalito, California, 1997.

[96] O. Talu, A.L. Myers, Molecular simulation of adsorption: Gibbs dividing surface and comparison with experiment, AIChE J. 47 (5) (2001) 1160–1168.

[97] G. Jajko, J.J. Gutiérrez-Sevillano, A. Sławek, M. Szufla, P. Kozyra, D. Matoga, W. Makowski, S. Calero, Water adsorption in ideal and defective UiO-66 structures, Microporous Mesoporous Mater. 330 (2022) 111555.

[98] W.M. Haynes, CRC Handbook of Chemistry and Physics, ninety first ed., CRC Press Inc., Boca Raton, FL, 2010, pp. 3–262.

[99] D. Frenkel, B. Smit, Understanding Molecular Simulation: From Algorithms to Applications, second ed., Academic Press, San Diego, CA, 2002.

[100] D.-Y. Peng, D.B. Robinson, A new two-constant equation of state, Ind. Eng. Chem. Fundam. 15 (1) (1976) 59–64.

[101] E.W. Lemmon, I.H. Bell, M.L. Huber, M.O. McLinden, NIST Standard Reference Database 23: Reference Fluid Thermodynamic and Transport Properties-REFPROP, Version 10.0, National Institute of Standards and Technology, 2018, URL https://www.nist.gov/srd/refprop.

[102] I. Matito-Martos, A. Rahbari, A. Martin-Calvo, D. Dubbeldam, T.J.H. Vlugt, S. Calero, Adsorption equilibrium of nitrogen dioxide in porous materials, Phys. Chem. Chem. Phys. 20 (2018) 4189–4199.

[103] J.R. Taylor, An Introduction to Error Analysis: The Study of Uncertainties in Physical Measurements, second ed., University Science Books, 1996.

[104] S. Builes, S.I. Sandler, R. Xiong, Isosteric heats of gas and liquid adsorption, Langmuir 29 (33) (2013) 10416–10422.

[105] D. Farrusseng, C. Daniel, C. Gaudillère, U. Ravon, Y. Schuurman, C. Mirodatos, D. Dubbeldam, H. Frost, R.Q. Snurr, Heats of adsorption for seven gases in three metal-organic frameworks: Systematic comparison of experiment and simulation, Langmuir 25 (13) (2009) 7383–7388.

[106] M.P. Allen, D.J. Tildesley, Computer Simulation of Liquids, second Ed., Oxford University Press, Oxford, UK, 2017.

[107] F.J. Salas, E. Nunez-Rojas, J. Alejandre, Stability of formic acid/pyridine and isonicotinamide/formamide cocrystals by molecular dynamics simulations, Theoret. Chem. Accounts 136 (1) (2017) 1–12.

[108] B.A. Wells, A.L. Chaffee, Ewald summation for molecular simulations, J. Chem. Theory Comput. 11 (8) (2015) 3684–3695.

[109] F. Darkrim, D. Levesque, Monte Carlo simulations of hydrogen adsorption in single-walled carbon nanotubes, J. Chem. Phys. 109 (12) (1998) 4981–4984.

[110] A. García-Sánchez, C.O. Ania, J.B. Parra, D. Dubbeldam, T.J.H. Vlugt, R. Krishna, S. Calero, Transferable force field for carbon dioxide adsorption in zeolites, J. Phys. Chem. C 113 (20) (2009) 8814–8820.

[111] S.L. Mayo, B.D. Olafson, W.A. Goddard, DREIDING: A generic force field for molecular simulations, J. Phys. Chem. 94 (26) (1990) 8897–8909.

[112] A.K. Rappe, C.J. Casewit, K.S. Colwell, W.A. Goddard, W.M. Skiff, UFF, a full periodic table force field for molecular mechanics and molecular dynamics simulations, J. Am. Chem. Soc. 114 (25) (1992) 10024–10035.

[113] D. Dubbeldam, K. Walton, D. Ellis, R. Snurr, Exceptional negative thermal expansion in isoreticular metal–organic frameworks, Angew. Chemie Int. Ed. 46 (24) (2007) 4496–4499.

[114] G. Jajko, P. Kozyra, J.J. Gutiérrez-Sevillano, W. Makowski, S. Calero, Carbon dioxide capture enhanced by pre-adsorption of water and methanol in UiO-66, Chem. – A Eur. J. 27 (59) (2021) 14653–14659.

[115] J.J. Gutiérrez-Sevillano, D. Dubbeldam, L. Bellarosa, N. López, X. Liu, T.J.H. Vlugt, S. Calero, Strategies to simultaneously enhance the hydrostability and the alcohol–water separation behavior of Cu-BTC, J. Phys. Chem. C 117 (40) (2013) 20706–20714.

[116] C.E. Wilmer, K.C. Kim, R.Q. Snurr, An extended charge equilibration method, J. Phys. Chem. Lett. 3 (17) (2012) 2506–2511.

[117] J.O. Hirschfelder, C.F. Curtiss, R.B. Bird, Molecular theory of gases and liquids, J. Wiley, New York, 1964.

[118] A. Martin-Calvo, J.J. Gutiérrez-Sevillano, I. Matito-Martos, T.J.H. Vlugt, S. Calero, Identifying zeolite topologies for storage and release of hydrogen, J. Phys. Chem. C 122 (23) (2018) 12485–12493.

[119] D. Dubbeldam, S. Calero, T.J.H. Vlugt, iRASPA: GPU-accelerated visualization software for materials scientists, Mol. Simul. 44 (8) (2018) 653–676.